



Zero-Field Nernst Effect in a Ferromagnetic Kagome-Lattice Weyl-Semimetal $\text{Co}_3\text{Sn}_2\text{S}_2$

Satya N. Guin,* Praveen Vir, Yang Zhang, Nitesh Kumar, Sarah J. Watzman, Chenguang Fu, Enke Liu, Kaustuv Manna, Walter Schnelle, Johannes Gooth, Chandra Shekhar, Yan Sun, and Claudia Felser*

The discovery of magnetic topological semimetals has recently attracted significant attention in the field of topology and thermoelectrics. In a thermoelectric device based on the Nernst geometry, an external magnet is required as an integral part. Reported is a zero-field Nernst effect in a newly discovered hard-ferromagnetic kagome-lattice Weyl-semimetal $\text{Co}_3\text{Sn}_2\text{S}_2$. A maximum Nernst thermopower of $\approx 3 \mu\text{V K}^{-1}$ at 80 K in zero field is achieved in this magnetic Weyl-semimetal. The results demonstrate the possibility of application of topological hard magnetic semimetals for low-power thermoelectric devices based on the Nernst effect and are thus valuable for the comprehensive understanding of transport properties in this class of materials.

The advantages such as the absence of moving parts and noise make the thermoelectric technology promising for energy conversion and solid-state cooling.^[1–6] Its progress largely relies on the Seebeck effect, i.e., the generation of an electrical voltage longitudinal to a temperature gradient. In contrast, configurations based on the Nernst effect, which is the generation of a transverse electrical signal in a magnetic field, have been significantly less studied,^[7–9] partly as an external magnetic field is usually required to observe a Nernst signal. In conventional thermoelectric devices based on the Seebeck effect, the heat reservoir

is required to be a part of the electrical circuit (Figure 1a). In contrast, the multi-terminal thermoelectric devices based on the Nernst effect enable spatial separation of the heat reservoir from the electric circuitry.^[10] Moreover, in Nernst devices, there is no need for both p- and n-type materials as the polarity of the voltage can be reversed by reversing the magnetic field direction.^[8,11] Therefore, Nernst devices overcome certain problems of Seebeck devices, where the different thermal expansion coefficients of p- and n-type materials lead to compatibility issues.

In a ferromagnetic material, the generation of an additional electric voltage orthogonal to the applied temperature gradient due to the internal magnetization is referred to as the anomalous Nernst effect (ANE).^[11,12] In general, the Nernst thermopower (S_{xy}) of a soft magnetic material is zero once the magnetic field is removed. Therefore, a part generating an external magnetic field needs to be integrated in devices based on the Nernst effect, which is a big obstacle for the thermomagnetic devices. A possible solution could be the use of a hard magnetic material, where an anomalous Nernst signal (S_{xy}^A) can be obtained in zero field. Such a permanent magnetic material remains in a magnetized state even when the external magnetic field is removed.^[13,14] Magnetic ferrites and rare-earth-based hard magnets have been extensively studied owing to their wide range of functional applications including magnetic motors, magnetic recording media, magnetic fluids, and electromagnetic wave filters.^[13–16] A novel potential application with hard magnets is energy conversion based on the Nernst effect, which has not attracted significant attention. Few examples of such materials include thin films of the alloys FePt, FePd, $\text{Li}_0\text{-MnGa}$, $\text{D}_{0.22}\text{-Mn}_2\text{Ga}$, Co/Ni, dilute magnetic semiconductor (DMS) $\text{Ga}_{1-x}\text{Mn}_x\text{As}$, and recently Mn_3Sn .^[17–20] Therefore, novel hard-magnetic materials are required. Studies on their thermomagnetic properties are of significance in terms of both technological application and fundamental understanding. A promising approach is to search for a new candidate from the library of topological materials as they share many mutual features with the thermoelectric materials.

In the current decade, topological materials attract significant research interest. These newly discovered materials exhibit various physical properties such as chiral anomaly, high carrier mobility, giant magnetoresistance, and mixed axial-gravitational anomaly due to the topological band structure.^[21–26] They are

Dr. S. N. Guin, P. Vir, Y. Zhang, Dr. N. Kumar, Dr. C. Fu, Dr. E. K. Liu, Dr. K. Manna, Dr. W. Schnelle, Dr. J. Gooth, Dr. C. Shekhar, Dr. Y. Sun, Prof. C. Felser
Department of Solid State Chemistry
Max Planck Institute for Chemical Physics of Solids
01187 Dresden, Germany
E-mail: satyanarayanguin@cpfs.mpg.de; Claudia.Felser@cpfs.mpg.de
Dr. S. J. Watzman
Department of Mechanical and Materials Engineering
University of Cincinnati
Cincinnati, OH 45221, USA
Dr. E. K. Liu
Institute of Physics
Chinese Academy of Sciences
Beijing 100190, China

The ORCID identification number(s) for the author(s) of this article can be found under <https://doi.org/10.1002/adma.201806622>.

© 2019 Max Planck Society. Published by WILEY-VCH Verlag GmbH & Co. KGaA, Weinheim. This is an open access article under the terms of the Creative Commons Attribution-NonCommercial License, which permits use, distribution and reproduction in any medium, provided the original work is properly cited and is not used for commercial purposes.

DOI: 10.1002/adma.201806622

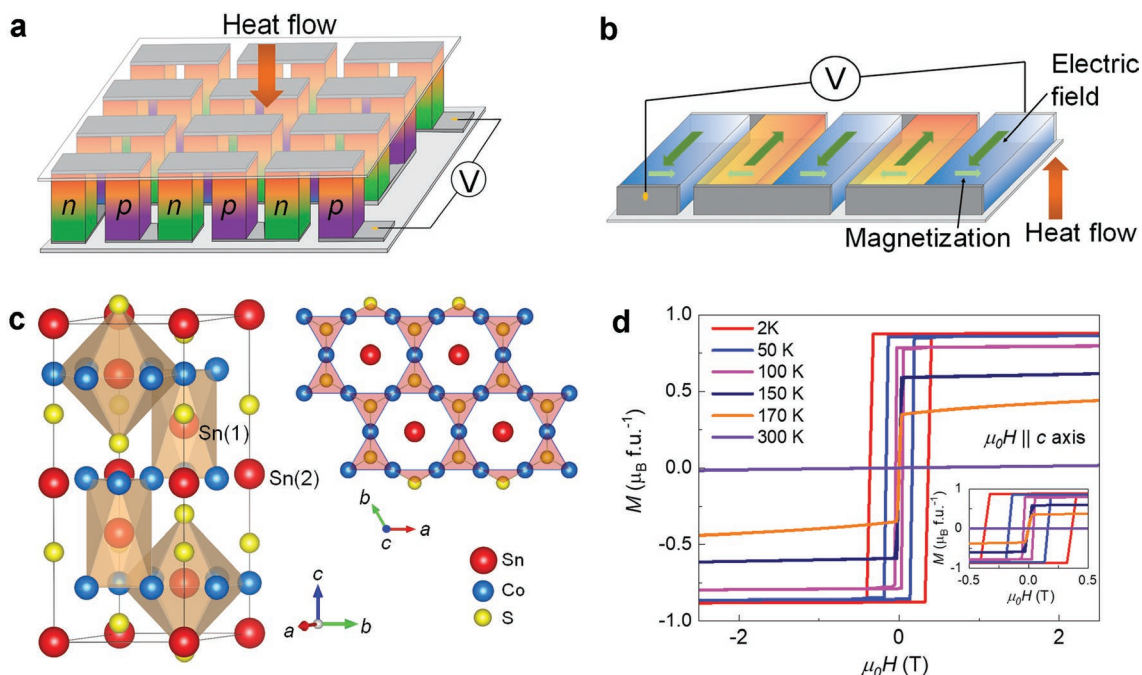


Figure 1. Schematics of thermoelectric modules, crystal structure, and magnetization of $\text{Co}_3\text{Sn}_2\text{S}_2$. a, b) Thermoelectric modules in the Seebeck and Nernst geometries, respectively. In the conventional Seebeck device, both n- and p-type legs are required. In contrast, in the Nernst device, a single type of thermopile can be used and the polarity of the voltage can be altered by changing the magnetization direction. c) Crystal structure of $\text{Co}_3\text{Sn}_2\text{S}_2$. Sn atoms are distributed over the interlayer (marked as Sn(1)) and in the kagome layers (marked as Sn(2)). The structure consists of the flat hexagonal kagome unit composed of Co and Sn(2) (see the *c*-axis view). The Sn(1) atoms are surrounded by a couple of Co_3 triangles in a trigonal-antiprismatic configuration. S atoms capped the Co_3 triangles above or below the kagome sheets. d) Field-dependent magnetization of $\text{Co}_3\text{Sn}_2\text{S}_2$ at different temperatures. The inset shows a magnified plot.

also potential candidates for functional applications in quantum computing, infrared sensors, and heterogenous catalysis.^[27–29] In this context, the discovery of magnetic topological materials created a new frontier in the field.^[30–37] These exotic magnetic topological materials provide a new scope in the thermoelectric research as the topological band structure effect can enhance the thermoelectric response.

Here, we show that the topological ferromagnets with large coercive fields (H_c) could be potential candidates for observation of the Nernst effect in zero field. As a case study material, we choose $\text{Co}_3\text{Sn}_2\text{S}_2$, a newly discovered hard-magnetic kagome-lattice Weyl-semimetal. Recently, a large intrinsic anomalous Hall conductivity (AHC) and giant anomalous Hall angle (AHA) have been observed in $\text{Co}_3\text{Sn}_2\text{S}_2$, originating from the topological band structure.^[38,39] We show that a single-crystalline $\text{Co}_3\text{Sn}_2\text{S}_2$ exhibits a maximum S_{xy}^A value of $\approx 3 \mu\text{V K}^{-1}$ at 80 K in zero field, which is significantly high considering its magnetic moment of $\approx 0.89 \mu_B \text{ f.u.}^{-1}$. We employed a combined approach including electrical and thermoelectric measurements and first-principles calculations to elucidate this observation. Our complementary electrical transport measurement and density functional theory (DFT)-based calculations indicate that the high Nernst signal in $\text{Co}_3\text{Sn}_2\text{S}_2$ originates from the topological band structure.

The ternary chalcogenide $\text{Co}_3\text{Sn}_2\text{S}_2$ is a member of the shandite family $A_3M_2X_2$ ($A = \text{Ni, Co, Rh, Pd}$; $M = \text{Pb, In, Sn, Tl}$; $X = \text{S, Se}$) and crystallizes in a rhombohedral structure (space group: $R\bar{3}m$).^[40,41] In this structure, Sn atoms are

distributed over interlayers (Sn1) and in the kagome layers (Sn2). The Sn(1) atoms are surrounded by two Co_3 triangles in a trigonal-antiprismatic configuration, whereas the Sn(2) atoms form a hexagonal planar layer with the magnetic Co atoms arranged on a kagome lattice in the *ab*-plane (Figure 1c). Each of the Co_3 triangles is capped above or below the kagome sheets by an S atom. The material is a type-IA half-metallic ferromagnet with a Curie temperature of $T_c = 177 \text{ K}$ and magnetic moment of $0.29 \mu_B/\text{Co}$.^[40,41] The strong magnetic anisotropy leads to a long-range quasi-2D type of magnetism with a spontaneous out-of-plane magnetization.^[40,41]

The single crystals of $\text{Co}_3\text{Sn}_2\text{S}_2$ were synthesized from the elements using a melting reaction followed by slow cooling. The as-grown crystal was characterized by Laue X-ray diffraction (XRD) and powder XRD (see the Experimental Section, and Figure S1, Supporting Information). For the electrical and thermoelectric measurements, the crystal was oriented and cut into a bar shape. As the material exhibits a highly anisotropic out-of-plane magnetization, we used the following configuration: magnetic field (μ_0H) \parallel *c*-axis and electrical current (I) or thermal gradient (ΔT) \parallel *ab*-plane.

Figure 1d shows the magnetization (M) as a function of the magnetic field (μ_0H) for $\text{Co}_3\text{Sn}_2\text{S}_2$ at different temperatures. Distinct rectangular-shaped hysteresis loops with large coercive fields H_c of ≈ 3650 and $\approx 570 \text{ Oe}$ are observed at 2 and 100 K, respectively. The origin of the large coercivity is attributed to the strong magnetic anisotropy of the compound (see Discussion, Supporting Information).^[42] This distinct hysteresis loop is observed up to $\approx 100 \text{ K}$; it becomes less pronounced with the further increase in

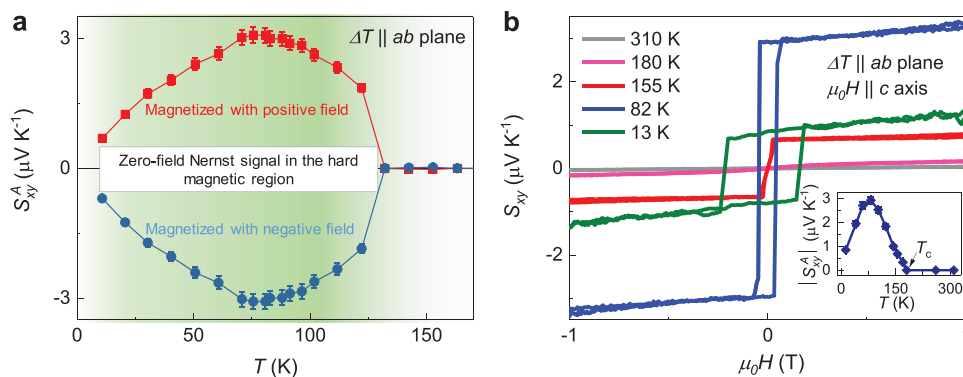


Figure 2. Nernst thermopower data. a) Temperature (T)-dependent anomalous Nernst thermopower (S_{xy}^A) of $\text{Co}_3\text{Sn}_2\text{S}_2$ in zero field, measured using a magnetized sample. b) Magnetic field dependences of the Nernst thermopower (S_{xy}) of $\text{Co}_3\text{Sn}_2\text{S}_2$ at different temperatures. The extracted zero-field anomalous Nernst thermopower (S_{xy}^A) as a function of T is presented in the inset.

temperature and vanishes as the temperature approaches T_c . The temperature-dependent magnetization measurement indicates a magnetic transition at ≈ 177 K (Figure S2, Supporting Information). Overall, the magnetic measurement data indicate that $\text{Co}_3\text{Sn}_2\text{S}_2$ exhibits a sizable H_c up to ≈ 120 K.

After we demonstrated the hard-magnetic nature of $\text{Co}_3\text{Sn}_2\text{S}_2$, we investigated the anomalous Nernst thermopower (S_{xy}^A) in zero magnetic field. We magnetized the sample by applying a field of ± 1 T ($>H_c$) to orient the magnetic moments along the c -axis and then switched off the field. Figure 2a presents S_{xy}^A of $\text{Co}_3\text{Sn}_2\text{S}_2$ in zero field as a function of the temperature. S_{xy}^A increases with the temperature and reaches a peak value of ≈ 3 $\mu\text{V K}^{-1}$ at ≈ 80 K. The further increase in the temperature leads to a decrease in S_{xy}^A ; above ≈ 120 K, the signal is almost zero as the compound loses its hard-magnetic structure. The observed maximum value of S_{xy}^A for $\text{Co}_3\text{Sn}_2\text{S}_2$ is remarkable considering the magnetic moment of ≈ 0.89 μ_B f.u. $^{-1}$ (see Discussion in the Supporting Information). Further, we investigated the magnetic-field dependence of the Nernst thermopower $S_{xy}(\mu_0H)$ at different temperatures (Figure 2b and Figure S4, Supporting Information). As discussed in the introduction that ferromagnets exhibit ANE below their T_C , this system starts to exhibit an anomalous behavior in S_{xy} . The effect of the large magnetocrystalline anisotropy of this compound is evident in the $S_{xy}(\mu_0H)$ data. The anomalous behavior in $S_{xy}(\mu_0H)$ (Figure 2b and Figure S4, Supporting Information) can be observed up to the Curie temperature of the compound ($T_C = 177$ K). Above T_C the $\text{Co}_3\text{Sn}_2\text{S}_2$ does not show any ANE as it is no longer magnetic in nature. Below 100 K, a rectangular-shaped hysteresis loop was observed in the $S_{xy}(\mu_0H)$ data; S_{xy} maintains a plateau value after a certain field. The change of the sign of S_{xy} is due to the flipping of the magnetic moment of the Co atoms with the direction of μ_0H (positive to negative). This observation is consistent with the zero-field measurement of a magnetized sample. The finite H_c in the data below ≈ 120 K enables to estimate the zero-field S_{xy} , i.e., S_{xy}^A . The temperature-dependent estimated values of S_{xy}^A from the field sweep data are in good agreement with the temperature-dependent zero-field measurement results (inset in Figure 2b). In the $S_{xy}(\mu_0H)$ data, we observed S_{xy}^A up to ≈ 170 K by extrapolating the slope of the high-field data; however, estimated S_{xy}^A above ≈ 120 K is not a true zero-field anomalous value, as the hard-magnetic nature disappears above ≈ 120 K.

In order to understand the origin of the large S_{xy}^A of $\text{Co}_3\text{Sn}_2\text{S}_2$, we measured the electrical resistivity (ρ_{xx}), longitudinal thermoelectric response, i.e., the Seebeck coefficient (S_{xx}), and Hall resistivity (ρ_{yx}). The temperature dependence of the electrical resistivity (ρ_{xx}) is presented in Figure 3a. ρ_{xx} decreases with the decrease in the temperature reaching a value of ≈ 55 $\mu\Omega$ cm at 2 K, indicating the metallic nature of the compound. The anomaly at $T_c = 177$ K in ρ_{xx} reflects the onset of a magnetic transition. The negative sign of S_{xx} is attributed to the dominant n-type charge carriers in $\text{Co}_3\text{Sn}_2\text{S}_2$ (Figure 3b). S_{xx} linearly increases with the temperature and becomes approximately constant in the range of 50–120 K. Above 120 K, S_{xx} increases with the temperature and exhibits an anomaly near T_c .

It is known that the intrinsic band structure effect from the Berry curvature can lead to a large anomalous Hall effect (AHE) in a topological material (see the Experimental Section). Therefore, we estimated the Hall conductivity (σ_{xy}) of $\text{Co}_3\text{Sn}_2\text{S}_2$ from the measured electrical resistivity (ρ_{xx}) and Hall resistivity (ρ_{yx})

$$\sigma_{xy} = \frac{\rho_{yx}}{\rho_{yx}^2 + \rho_{xx}^2} \quad (1)$$

Figure 3c presents σ_{xy} of $\text{Co}_3\text{Sn}_2\text{S}_2$ as a function of the magnetic field at different temperatures. The trend and values of the AHC (σ_{xy}^A) are fully consistent with previous observations.^[38] Below 100 K, a large AHE is observed with a sharp rectangular-shaped loop, which arises from the topological-band-structure-enhanced Berry curvature effect.^[38] This observation indicates the topological-band-structure-related origin of the large S_{xy}^A of $\text{Co}_3\text{Sn}_2\text{S}_2$ as the transverse thermoelectric response is associated with the Berry curvature, as discussed below.

The notion of the topological band structure effect in transverse thermoelectric responses can be understood by analyzing the temperature dependence of the anomalous transverse thermoelectric conductivity (α_{xy}^A). Therefore, we estimated the transverse thermoelectric conductivity (α_{yx}) using the measured components of resistivity (ρ_{xx} , ρ_{yx}) and Seebeck and Nernst thermopowers (S_{xx} and $S_{xy} = -S_{yx}$)

$$\alpha_{yx} = \frac{S_{yx}\rho_{xx} - S_{xx}\rho_{yx}}{\rho_{xx}^2 + \rho_{yx}^2} \quad (2)$$

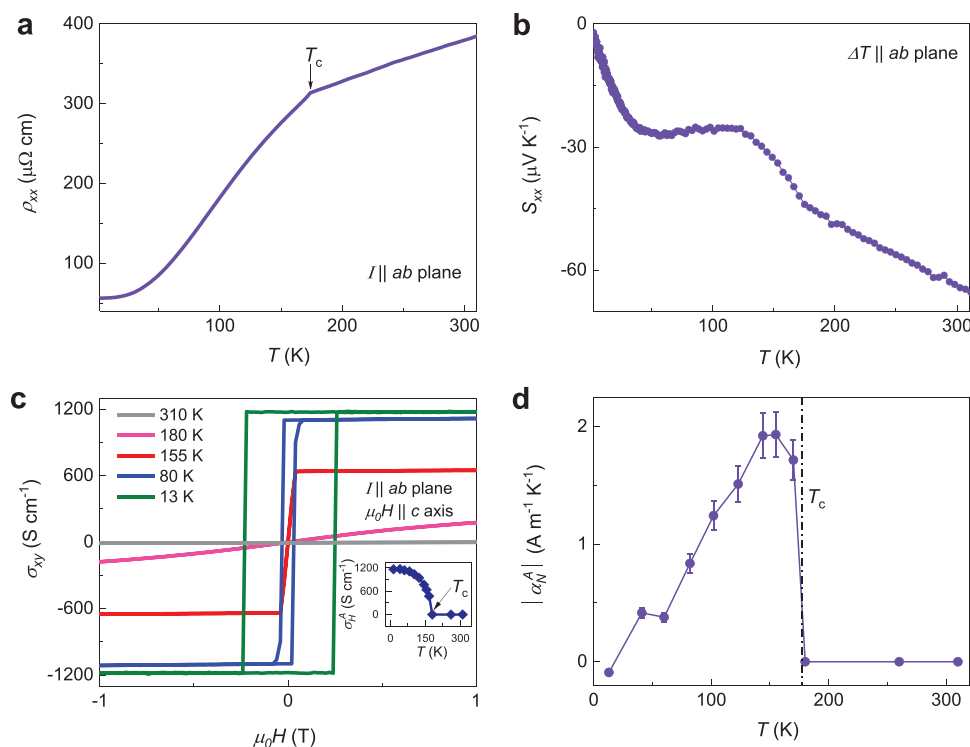


Figure 3. Electrical transport, Seebeck coefficient, and thermoelectric conductivity. a) T -dependent electrical resistivity (ρ_{xx}). The change in slope in ρ_{xx} around ≈ 177 K corresponds to a magnetic transition (marked with an arrow). b) T dependence of the Seebeck coefficient (S_{xx}) of $\text{Co}_3\text{Sn}_2\text{S}_2$. c) Magnetic field dependence of the Hall conductivity (σ_{xy}). The T dependence of the AHC (σ_H^A) is shown in the inset. d) T dependence of the experimentally determined anomalous transverse thermoelectric conductivity (α_N^A). The dotted line indicates magnetic transition temperature.

Figure 3d shows the anomalous part of α_{yx} of $\text{Co}_3\text{Sn}_2\text{S}_2$. The S_{xy} and ρ_{yx} exhibit anomalous behavior below T_C . Therefore, a nonzero α_N^A value can be observed only below T_C . In $\text{Co}_3\text{Sn}_2\text{S}_2$, the α_N^A shows a peak value around 150 K and decreases upon cooling, although the saturation magnetization increases. A similar observation was reported in an anomalous Hall resistance measurement.^[38] The observation is an evidence that the anomalous Nernst signal originates from a different source, rather than from the magnetization.

For a deeper understanding, we carried out DFT- and ab-initio-based electronic structure calculations and numerical simulations of σ_H^A and α_N^A using the Kubo formula. **Figure 4a** shows the calculated electronic structures of $\text{Co}_3\text{Sn}_2\text{S}_2$ with and without spin-orbit coupling (SOC). The spin-down channel of the bands has a gap of ≈ 0.35 eV, while the spin-up channel is semimetallic (see also Figure S6, Supporting Information). Moreover, for the spin-up channel along the Γ -L and L-U paths, linear band crossings can be observed near the charge-neutral Fermi point (E_0). In the absence of SOC, the full Hamiltonian could be split into the direct product of a spinless Hamiltonian and spin-Hamiltonian, in which the band degeneracy of each spin channel is determined by the spinless Hamiltonian. Owing to the mirror symmetry of the lattice, the band inversion of the spin-up channel forms a nodal line in the mirror plane (M_y). Considering the combination of inversion and C_3 rotational symmetries, there are six nodal lines in total (Figure 4b). The application of SOC breaks the mirror symmetry and lifts the degeneracy of the nodal lines, with one pair of Weyl points remaining on it.

Figure 4c shows the computed α_N^A as a function of the position of the Fermi level (E_F) at 80 K. We would like to note that unlike intrinsic AHE, the intrinsic part of α_N^A depends on the strength of the Berry curvature near E_F rather than on the Berry curvature of all of the occupied bands (see the Experimental Section).^[43,44] The anomalous Nernst conductivity (ANC) of $\text{Co}_3\text{Sn}_2\text{S}_2$ exhibits a strong E_F dependence, which is not observed for σ_H^A (Figure S7, Supporting Information). σ_H^A maintains a plateau value (≈ 1000 S cm^{-1}) over an energy window of ≈ 100 meV around E_F . In contrast, α_N^A has a peak value slightly away from E_F and then rapidly decreases away from E_F due to the modulation of the Berry curvature strength. This finding was further supported by our temperature-dependent σ_H^A and α_N^A data. The experimental σ_H^A exhibits a small change below ≈ 100 K. In contrast, α_N^A exhibits a monotonous decreasing trend with the decrease in temperature.

In a previous study, angle-resolved photoelectron spectroscopy and low-temperature Shubnikov-de Haas quantum oscillation analysis indicated that E_F was slightly shifted toward the valence bands in $\text{Co}_3\text{Sn}_2\text{S}_2$.^[38] In this study, we use a sample with a similar quality to that for the AHE, indicating a similar position of E_F . We calculated the temperature dependence of α_N^A below ordering temperature using different positions of E_F of $\text{Co}_3\text{Sn}_2\text{S}_2$ (Figure S8, Supporting Information). α_N^A exhibits a monotonous increase with T for $E_F = E_0 - 0.07$ eV to $E_0 - 0.10$ eV and well agrees with the experimental value when $E_F = E_0 - 0.08$ eV (Figure 4d). Moreover, the temperature-modified Berry curvature distributions (Ω_N) at 80 and 150 K for $E_F = E_0 - 0.08$ eV

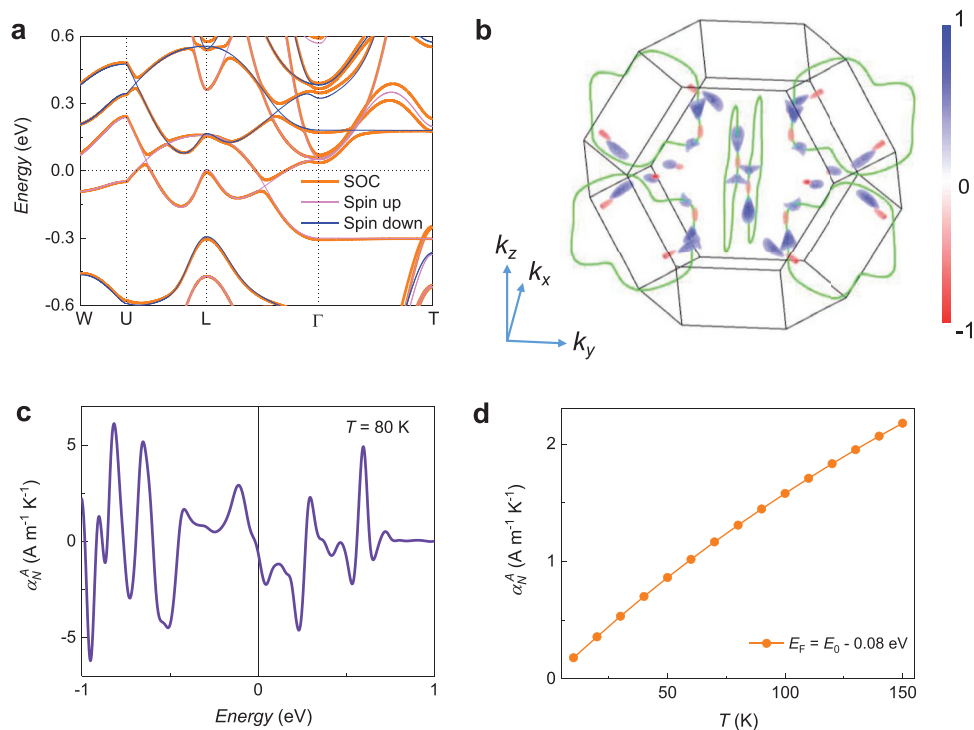


Figure 4. Electronic structure and calculated transverse thermoelectric conductivity. a) Electronic structures of $\text{Co}_3\text{Sn}_2\text{S}_2$ with and without SOC. The application of SOC breaks the mirror symmetry leading to gapping of the nodal lines due to the degeneracy lifting of the bands. b) Temperature-modified Berry curvature distribution (Ω_N) at 80 K in the Brillouin zone with the magnetization along the c -axis for $E_F = E_0 - 0.08$ eV. The green lines indicate the nodal rings. c) Theoretically calculated ANC (α_N^A) as a function of the chemical potential with respect to the charge neutrality point E_0 at $T = 80$ K. d) Theoretically estimated temperature-dependent α_N^A with $E_F = E_0 - 0.08$ eV below ordering temperature. The calculated value is in good agreement with the measured value.

also have large nonzero values (Figure 4b and Figure S9, Supporting Information), suggesting a topological band structure contribution in the transverse thermoelectric transport.

Figure 5 compares the absolute value of peak S_{xy}^A of different class of materials from the literature with $\text{Co}_3\text{Sn}_2\text{S}_2$.^[17–19,34,45–49] A maximum S_{xy}^A of $\approx 3 \mu\text{V K}^{-1}$ at $T = 80$ K is measured in the case of $\text{Co}_3\text{Sn}_2\text{S}_2$. In addition, $\text{Co}_3\text{Sn}_2\text{S}_2$

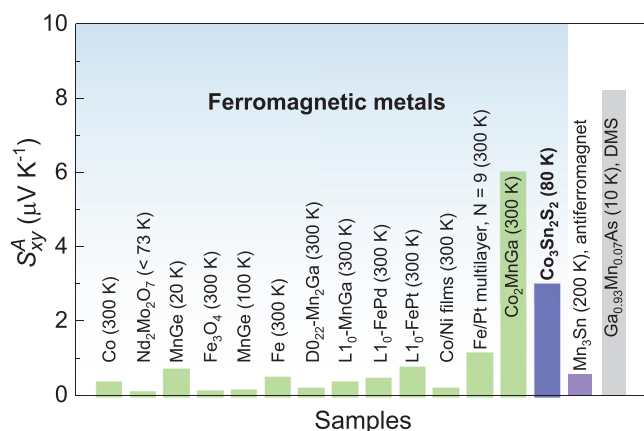


Figure 5. Absolute value of anomalous Nernst thermopowers (S_{xy}^A) for ferromagnetic metals, antiferromagnet Mn_3Sn , DMS $\text{Ga}_{0.93}\text{Mn}_{0.07}\text{As}$ from the literature and $\text{Co}_3\text{Sn}_2\text{S}_2$. The shaded region indicates hard and soft ferromagnetic metals.^[17–19,34,45–49]

exhibits a zero-field signal, which is not the case for nonmagnetic and soft-ferromagnetic metals. Although the maximum S_{xy}^A of $\text{Co}_3\text{Sn}_2\text{S}_2$ ($\approx 3 \mu\text{V K}^{-1}$ at $T = 80$ K) is lower than that of topological ferromagnet Co_2MnGa ($\approx 6 \mu\text{V K}^{-1}$ at $T = 300$ K) and DMS $\text{Ga}_{0.93}\text{Mn}_{0.07}\text{As}$ ($\approx 8.1 \mu\text{V K}^{-1}$ at $T = 10$ K), but the present results provide a possible guiding principle for the observation of large zero-field anomalous Nernst thermopower in a hard-ferromagnetic topological semimetal at elevated temperature. Moreover, considering the magnetic moments of $\approx 0.79 \mu_B \text{ f.u.}^{-1}$ for $\text{Co}_3\text{Sn}_2\text{S}_2$ ($T = 80$ K) and $\approx 3.7 \mu_B \text{ f.u.}^{-1}$ for Co_2MnGa ($T = 300$ K), the present result is more interesting and due to lower magnetic moment the inherent stray field for $\text{Co}_3\text{Sn}_2\text{S}_2$ will be low. Figure S10 in the Supporting Information compares the ratios of the strengths of the anomalous Nernst signals to their saturation magnetizations of different hard and soft ferromagnetic metals and antiferromagnet Mn_3Sn .^[17,19,34,45–49] The Y-axis of the plot (S_{xy}^A/μ_0M) represents the ratio of S_{xy}^A to the magnetic moment (μ_0M). The values of S_{xy}^A/μ_0M for the topological ferromagnets are higher than those of the trivial ferromagnetic materials. A similar result was observed for the topological chiral antiferromagnet Mn_3Sn ; however, it exhibited a lower Nernst signal than that of $\text{Co}_3\text{Sn}_2\text{S}_2$ (Figure S10, Supporting Information).^[19] S_{xy}^A/μ_0M indicates that the strength of the transverse signal is significantly higher in $\text{Co}_3\text{Sn}_2\text{S}_2$ and indeed highest among those of ferromagnetic metals. This implies that the anomalous transport properties originate from the topological band structure effect and are independent of the strength of the magnetic moments.

In conclusion, magnetic topological semimetals are potential candidates for the observation of exotic anomalous transport properties. We showed that the hard ferromagnetic kagome-lattice Weyl-semimetal $\text{Co}_3\text{Sn}_2\text{S}_2$ from the shandite family exhibited a large ANE in zero field. Our experimental and DFT calculation results showed that the large ANE originated from the strong Berry curvature was associated with the nodal lines and Weyl points. Although the magnitude of the zero-field transverse signal of $\text{Co}_3\text{Sn}_2\text{S}_2$ was not sufficiently high for applications, this study shows that the topological material with a large H_c could be a potential candidate for a transverse thermoelectric and that the large signal can be achieved in zero field. Therefore, it is of interest to search for new hard magnets with high Curie temperatures from the library of magnetic topological materials.

Experimental Section

Single-Crystal Growth of $\text{Co}_3\text{Sn}_2\text{S}_2$ and Characterization: The single crystals of $\text{Co}_3\text{Sn}_2\text{S}_2$ were grown using an elemental melting reaction followed by a slow cooling. As-purchased high-quality elemental cobalt (99.999%), tin (99.999%), and sulfur (99.999%) were used for the synthesis. Stoichiometric amounts of the elements (Co:Sn:S = 3:2:2) were loaded in an alumina crucible and then sealed in a quartz tube. The tube was heated to 1323 K over a period of 48 h, soaked for 24 h, and then slowly cooled down to 873 K over 7 days. The power XRD measurement was performed at room temperature using a Huber Image Plate Guinier Camera G670 operated with Cu $K_{\alpha 1}$ radiation ($\lambda = 1.54056 \text{ \AA}$). The single crystallinity of the as-grown crystal was evaluated by the white-beam backscattering Laue XRD method. Well-characterized and aligned crystals were cut into bar shapes for transport and magnetization measurements. The typical dimensions of the crystals used for the electrical and thermal transport measurements were $\approx 7 \times 1.3 \times 0.4 \text{ mm}^3$.

Electrical Transport and Magnetization Measurements: The electrical transport properties were measured using a PPMS9 instrument (ACT option, Quantum Design). The standard four-probe method was used in all of the measurements. In order to correct for contact misalignment, the measured data were field-symmetrized and antisymmetrized. The magnetization measurement was performed using a Quantum Design MPMS3 instrument.

Thermoelectric Transport Measurements: All of the thermal transport experiments were performed in a physical property measurement system (PPMS) cryostat. The Seebeck and Nernst thermoelectric measurements were carried out in the one-heater two-thermometer configuration. In the field sweep experiments in a temperature range of 13–310 K, the PPMS as well as an external nanovoltmeter and current source (Keithley) were controlled using LabVIEW. The temperature gradient was generated using a resistive heater, connected to a gold-coated flat copper wire at one end of the sample. The thermal gradient ΔT was applied along the *ab*-plane of the sample, while the magnetic field was applied along the *c*-axis. Another gold-plated flat copper wire was attached to the puck clamp for the heat sink. In order to measure the temperature gradient, two gold-plated copper leads were attached directly to the sample using a silver-filled epoxy along the thermal gradient direction. The distance between the thermometers was $\approx 3.5 \text{ mm}$. In the Seebeck and Nernst measurements, ΔT was typically set to ≈ 1 –3% of the base temperature. Two copper wires were attached using the silver epoxy, orthogonal to the thermal gradient direction, to measure the transverse voltage. In order to correct the data for contact misalignment, the measured data were field-symmetrized and antisymmetrized. The thermal conductivity measurement was carried out in the PPMS using the thermal transport option.

Anomalous Nernst Thermopower of Different Class of Materials from the Literature: The highest absolute value of anomalous Nernst thermopowers (S_{xy}^A) were used for the different soft and hard ferromagnets, antiferromagnet Mn_3Sn , and DMS $\text{Ga}_{0.93}\text{Mn}_{0.07}\text{As}$ well

below their Curie temperatures. Their magnetizations ($\mu_0 M$ in Tesla) were used to calculate the ratios (Co/Ni film (300 K; ref. [17]), $\text{L1}_0\text{-FePt}$ (300 K; ref. [17]), $\text{D0}_{22}\text{-Mn}_2\text{Ga}$ (300 K; ref. [17]), $\text{L1}_0\text{-MnGa}$ (300 K; ref. [17]), $\text{L1}_0\text{-FePd}$ (300 K; ref. [17]), $\text{Ga}_{0.93}\text{Mn}_{0.07}\text{As}$ (10 K, ref. [18]), Mn_3Sn (200 K; ref. [19]), Co_2MnGa (300 K; refs. [34,36]), $\text{Nd}_2\text{Mo}_2\text{O}_7$ ($T < T_c = 73 \text{ K}$, $B = 1 \text{ T}$ [111]; ref. [45]), Fe (300 K; ref. [46]), Co (300 K; ref. [46]), Fe_3O_4 (300 K, $B < 0.8 \text{ T}$; ref. [47]), MnGe (100 K, $B > 5 \text{ T}$; ref. [48]), and Pt/Fe multilayer ($N = 9$, 300 K, $B < 5 \text{ T}$; ref. [49]).

Ab Initio Calculations: For ab initio calculations, the DFT was employed using the Vienna ab initio simulation package,^[50] including the exchange–correlation energy through the Perdew–Burke–Ernzerhof functional. For the integrations in the *k*-space, a grid of $19 \times 19 \times 19$ points was used. The Wannier functions from the resulting band structure was extracted using WANNIER90^[51] to set up a tight-binding Hamiltonian, which reproduced the DFT band structure within a few millielectronvolts. With this Hamiltonian, the Berry curvature Ω_n was calculated

$$\Omega_{n,ij} = \text{Im} \sum_{m \neq n} \frac{\langle n | \frac{\partial H}{\partial k_i} | m \rangle \langle m | \frac{\partial H}{\partial k_j} | n \rangle}{(\epsilon_n - \epsilon_m)^2} - (i \leftrightarrow j) \quad (3)$$

where *m* and *n* are the eigenstates and ϵ are the eigenenergies of the Hamiltonian *H*.

Subsequently, the AHC σ_H^A was calculated as

$$\sigma_H^A = -\frac{e^2}{\hbar} \sum_n \int \frac{dk}{(2\pi)^3} \Omega_{n,xy}(k) f_{nk} \quad (4)$$

where f_{nk} is the Fermi–Dirac distribution for a band *n* at a *k*-point. The ANC α_N^A below ordering temperature is^[43]

$$\alpha_N^A = \frac{e}{T\hbar} \int \frac{dk}{(2\pi)^3} \Omega_N \quad (5)$$

If $\beta = k_B T$ was defined, where k_B is the Boltzmann constant, the temperature-modified Berry curvature distribution can be expressed as

$$\Omega_N = \sum_n \Omega_{n,xy}(k) \left\{ (\epsilon_{nk} - \mu) f_{nk} + k_B T \ln [1 + e^{-\beta(\epsilon_{nk} - \mu)}] \right\} \quad (6)$$

Ω_N has a finite value only around the Fermi energy. Therefore, σ_H^A is related to the summation of the Berry curvatures of all of the occupied bands below the Fermi energy. In contrast, α_N^A is related to the Berry curvature of the occupied bands near the Fermi energy. For the integrations over the whole Brillouin zone in the AHE and ANE calculations, a mesh of $251 \times 251 \times 251$ *k*-points was employed, providing converged results. Discussion on finite-temperature DFT calculation has been given in the Supporting Information.

Supporting Information

Supporting Information is available from the Wiley Online Library or from the author.

Acknowledgements

This study was financially supported by the ERC Advanced grant no. (742068) “TOP-MAT”, and Deutsche Forschungsgemeinschaft DFG under SFB 1143. S.N.G., Ch.F., and E.K.L. thank the Alexander von Humboldt Foundation for the fellowships. E.K.L. also thanks the National Natural Science Foundation of China (no. 51722106).

Conflict of Interest

The authors declare no conflict of interest.

Keywords

hard magnets, magnetic Weyl-semimetals, Nernst effect, thermoelectrics, zero-field Nernst thermopower

Received: October 12, 2018

Revised: April 2, 2019

Published online: May 1, 2019

- [1] D. M. Rowe, *CRC Handbook of Thermoelectrics*, CRC Press, Boca Raton, FL, USA 1995.
- [2] J. He, T. M. Tritt, *Science* **2017**, *357*, 1369.
- [3] G. J. Snyder, E. S. Toberer, *Nat. Mater.* **2008**, *7*, 105.
- [4] G. Tan, L.-D. Zhao, M. G. Kanatzidis, *Chem. Rev.* **2016**, *116*, 12123.
- [5] T. Zhu, Y. Liu, C. Fu, J. P. Heremans, G. J. Snyder, X. Zhao, *Adv. Mater.* **2017**, *29*, 1605884.
- [6] K. Biswas, J. He, I. D. Blum, C.-I. Wu, T. P. Hogan, D. N. Seidman, V. P. Dravid, M. G. Kanatzidis, *Nature* **2012**, *489*, 414.
- [7] K. Behnia, H. Aubin, *Rep. Prog. Phys.* **2016**, *79*, 046502.
- [8] S. J. Watzman, T. M. McCormick, C. Shekhar, S.-C. Wu, Y. Sun, A. Prakash, C. Felser, N. Trivedi, J. Heremans, *Phys. Rev. B* **2018**, *97*, 161404.
- [9] C. Fu, S. N. Guin, S. J. Watzman, G. Li, E. Liu, N. Kumar, V. Süß, W. Schnelle, G. Auffermann, C. Shekhar, Y. Sun, J. Gooth, C. Felser, *Energy Environ. Sci.* **2018**, *11*, 2813.
- [10] H. Thierschmann, R. Sánchez, B. Sothmann, F. Arnold, C. Heyn, W. Hansen, H. Buhmann, L. W. Molenkamp, *Nat. Nanotechnol.* **2015**, *10*, 854.
- [11] S. R. Boona, R. C. Myers, J. P. Heremans, *Energy Environ. Sci.* **2014**, *7*, 885.
- [12] T. Miyasato, N. Abe, T. Fujii, A. Asamitsu, S. Onoda, Y. Onose, N. Nagaosa, Y. Tokura, *Phys. Rev. Lett.* **2007**, *99*, 086602.
- [13] J. M. D. Coey, *IEEE Trans. Magn.* **2011**, *47*, 4671.
- [14] S. Hirotsawa, M. Nishino, S. Miyashita, *Adv. Nat. Sci. Nanosci. Nanotechnol.* **2017**, *8*, 013002.
- [15] A. Namai, M. Yoshikiyo, K. Yamada, S. Sakurai, T. Goto, T. Yoshida, T. Miyazaki, M. Nakajima, T. Suemoto, H. Tokoro, S. I. Ohkoshi, *Nat. Commun.* **2012**, *3*, 1035.
- [16] J. Jin, S. I. Ohkoshi, K. Hashimoto, *Adv. Mater.* **2004**, *16*, 48.
- [17] K. Hasegawa, M. Mizuguchi, Y. Sakuraba, T. Kamada, T. Kojima, T. Kubota, S. Mizukami, T. Miyazaki, K. Takanashi, *Appl. Phys. Lett.* **2015**, *106*, 252405.
- [18] Y. Pu, D. Chiba, F. Matsukura, H. Ohno, J. Shi, *Phys. Rev. Lett.* **2008**, *101*, 117208.
- [19] M. Ikhlas, T. Tomita, T. Koretsune, M. T. Suzuki, D. Nishio-Hamane, R. Arita, Y. Otani, S. Nakatsuji, *Nat. Phys.* **2017**, *13*, 1085.
- [20] X. Li, L. Xu, L. Ding, J. Wang, M. Shen, X. Lu, Z. Zhu, K. Behnia, *Phys. Rev. Lett.* **2017**, *119*, 056601.
- [21] M. Hirschberger, S. Kushwaha, Z. Wang, Q. Gibson, S. Liang, C. A. Belvin, B. A. Bernevig, R. J. Cava, N. P. Ong, *Nat. Mater.* **2016**, *15*, 1161.
- [22] T. Liang, Q. Gibson, M. N. Ali, M. Liu, R. J. Cava, N. P. Ong, *Nat. Mater.* **2015**, *14*, 280.
- [23] C. Shekhar, A. K. Nayak, Y. Sun, M. Schmidt, M. Nicklas, I. Leermakers, U. Zeitler, Y. Skourski, J. Wosnitza, Z. Liu, Y. Chen, W. Schnelle, H. Borrmann, Y. Grin, C. Felser, B. Yan, *Nat. Phys.* **2015**, *11*, 645.
- [24] F. Arnold, C. Shekhar, S. C. Wu, Y. Sun, R. D. Dos Reis, N. Kumar, M. Naumann, M. O. Ajeesh, M. Schmidt, A. G. Grushin, J. H. Bardarson, M. Baenitz, D. Sokolov, H. Borrmann, M. Nicklas, C. Felser, E. Hassinger, B. Yan, *Nat. Commun.* **2016**, *7*, 11615.
- [25] N. Kumar, Y. Sun, N. Xu, K. Manna, M. Yao, V. Süß, I. Leermakers, O. Young, T. Förster, M. Schmidt, H. Borrmann, B. Yan, U. Zeitler, M. Shi, C. Felser, C. Shekhar, *Nat. Commun.* **2017**, *8*, 1642.
- [26] J. Gooth, A. C. Niemann, T. Meng, A. G. Grushin, K. Landsteiner, B. Gotsmann, F. Menges, M. Schmidt, C. Shekhar, V. Süß, R. Hühne, B. Rellinghaus, C. Felser, B. Yan, K. Nielsch, *Nature* **2017**, *547*, 324.
- [27] L. M. Schoop, F. Pielhofer, B. V. Lotsch, *Chem. Mater.* **2018**, *30*, 3155.
- [28] C. R. Rajamathi, U. Gupta, N. Kumar, H. Yang, Y. Sun, V. Süß, C. Shekhar, M. Schmidt, H. Blumtritt, P. Werner, B. Yan, S. Parkin, C. Felser, C. N. R. Rao, *Adv. Mater.* **2017**, *29*, 1606202.
- [29] C.-K. Chan, N. H. Lindner, G. Refael, P. A. Lee, *Phys. Rev. B* **2017**, *95*, 41104.
- [30] Z. Wang, M. G. Vergniory, S. Kushwaha, M. Hirschberger, E. V. Chulkov, A. Ernst, N. P. Ong, R. J. Cava, B. A. Bernevig, *Phys. Rev. Lett.* **2016**, *117*, 236401.
- [31] K. Kuroda, T. Tomita, M.-T. Suzuki, C. Bareille, A. A. Nugroho, P. Goswami, M. Ochi, M. Ikhlas, M. Nakayama, S. Akebi, R. Noguchi, R. Ishii, N. Inami, K. Ono, H. Kumigashira, A. Varykhalov, T. Muro, T. Koretsune, R. Arita, S. Shin, T. Kondo, S. Nakatsuji, *Nat. Mater.* **2017**, *16*, 1090.
- [32] K. Manna, L. Muechler, T.-H. Kao, R. Stinshoff, Y. Zhang, N. Kumar, G. Kreiner, K. Koepf, R. Car, J. Kübler, G. H. Fecher, C. Shekhar, Y. Sun, C. Felser, *Phys. Rev. X* **2018**, *8*, 041045.
- [33] I. Belopolski, D. S. Sanchez, G. Chang, K. Manna, B. Ernst, S.-Y. Xu, S. S. Zhang, H. Zheng, J. Yin, B. Singh, G. Bian, D. Multer, X. Zhou, S.-M. Huang, B. Wang, A. Bansil, H. Lin, C. Felser, M. Z. Hasan, **2017**, *arXiv:1712.09992*.
- [34] S. N. Guin, K. Manna, J. Noky, S. J. Watzman, C. Fu, N. Kumar, W. Schnelle, C. Shekhar, Y. Sun, J. Gooth, C. Felser, *NPG Asia Mater.* **2019**, *11*, 16.
- [35] J. Noky, J. Gooth, C. Felser, Y. Sun, *Phys. Rev. B* **2018**, *98*, 241106(R).
- [36] A. Sakai, Y. P. Mizuta, A. A. Nugroho, R. Sihombing, T. Koretsune, M. T. Suzuki, N. Takemori, R. Ishii, D. Nishio-Hamane, R. Arita, P. Goswami, S. Nakatsuji, *Nat. Phys.* **2018**, *14*, 1119.
- [37] G. Chang, S. Y. Xu, H. Zheng, B. Singh, C. H. Hsu, G. Bian, N. Alidoust, I. Belopolski, D. S. Sanchez, S. Zhang, H. Lin, M. Z. Hasan, *Sci. Rep.* **2016**, *6*, 38839.
- [38] E. Liu, Y. Sun, N. Kumar, L. Muechler, A. Sun, L. Jiao, S. Y. Yang, D. Liu, A. Liang, Q. Xu, J. Kroder, V. Süß, H. Borrmann, C. Shekhar, Z. Wang, C. Xi, W. Wang, W. Schnelle, S. Wirth, Y. Chen, S. T. B. Goennenwein, C. Felser, *Nat. Phys.* **2018**, *14*, 1125.
- [39] Q. Wang, Y. Xu, R. Lou, Z. Liu, M. Li, Y. Huang, D. Shen, H. Weng, S. Wang, H. Lei, *Nat. Commun.* **2018**, *9*, 3681.
- [40] R. Wehrich, I. Anusca, *Z. Anorg. Allg. Chem.* **2006**, *632*, 1531.
- [41] P. Vaqueiro, G. G. Sobany, *Solid State Sci.* **2009**, *11*, 513.
- [42] R. Wehrich, W. Yan, J. Rothballer, P. Peter, S. M. Rommel, S. Haumann, F. Winter, C. Schwickert, R. Pöttgen, *Dalton Trans.* **2015**, *44*, 15855.
- [43] D. Xiao, Y. Yao, Z. Fang, Q. Niu, *Phys. Rev. Lett.* **2006**, *97*, 026603.
- [44] D. Xiao, M. C. Chang, Q. Niu, *Rev. Mod. Phys.* **2010**, *82*, 1959.
- [45] N. Hanasaki, K. Sano, Y. Onose, T. Ohtsuka, S. Iguchi, I. Kézsmárki, S. Miyasaka, S. Onoda, N. Nagaosa, Y. Tokura, *Phys. Rev. Lett.* **2008**, *100*, 106601.
- [46] J. Weischenberg, F. Freimuth, S. Blügel, Y. Mokrousov, *Phys. Rev. B* **2013**, *87*, 060406.
- [47] R. Ramos, M. H. Aguirre, A. Anadón, J. Blasco, I. Lucas, K. Uchida, P. A. Algarabel, L. Morellón, E. Saitoh, M. R. Ibarra, *Phys. Rev. B* **2014**, *90*, 054422.
- [48] Y. Shiomi, N. Kanazawa, K. Shibata, Y. Onose, Y. Tokura, *Phys. Rev. B* **2013**, *88*, 064409.
- [49] K. I. Uchida, T. Kikkawa, T. Seki, T. Oyake, J. Shiomi, Z. Qiu, K. Takanashi, E. Saitoh, *Phys. Rev. B* **2015**, *92*, 094414.
- [50] G. Kresse, J. Furthmüller, *Phys. Rev. B* **1996**, *54*, 11169.
- [51] A. A. Mostofi, J. R. Yates, Y.-S. Lee, I. Souza, D. Vanderbilt, N. Marzari, *Comput. Phys. Commun.* **2008**, *178*, 685.